Mercury wetting film on sapphire

Y. Ohmasa, Y. Kajihara, and M. Yao
Department of Physics, Graduate School of Science, Kyoto University, Kyoto 606-8502, Japan
(Received 28 August 2000; published 10 April 2001)

We have measured optical properties of a mercury wetting film on sapphire under high temperature and high pressure near the liquid-gas critical point of mercury by using a newly developed 45° reflection technique. We have analyzed the experimental data to deduce the density, the thickness, and the coverage of the wetting film quantitatively as functions of pressure and temperature. As a first approximation, we have assumed a slab model for the density profile of the wetting film, and found that the density of the wetting film d_{slab} is much smaller than that of bulk liquid at the liquid-vapor coexistence curve. This result is consistent with the Lifshitz theory, from which we may predict that the sapphire substrate prefers wetting film with density lower than the metal-nonmetal transition. When the temperature is close enough to the prewetting critical temperature T_{pw}^{c}, the effective slab density d_{slab} shows a sharp decrease as the pressure approaches the liquid-gas coexistence. This indicates that the slab model is not sufficient to describe the shape of the wetting film, and a smooth variation of the density has to be taken into account. In the prewetting supercritical region, two anomalies are observed in the reflectances. Possible mechanisms of these anomalies are discussed.

DOI: 10.1103/PhysRevE.63.051601 PACS number(s): 68.08.Bc, 68.15.+e

I. INTRODUCTION

It is well known that liquid mercury is a nonwetting substance on solid nonmetallic substrate under ambient conditions. Indeed the closest example in common experience of a nonwetting substance is a mercury drop on a glass plate. However, at high temperatures and high pressures close to the liquid-vapor critical point of mercury ($T_c = 1478\,^{\circ}\mathrm{C}$, $p_c = 167$ MPa, $d_c = 5.8$ g/cm^3), a transition from nonwetting to wetting is expected to take place from Cahn's critical-point wetting theory [1]. This transition is called a wetting transition. Cahn argued the asymptotic behavior of the Young's equation on approaching the liquid-gas critical point. Based on the scaling behavior of surface free energy, he predicted the necessity of wetting at the critical point.

The wetting transition of fluid mercury on a sapphire surface is found by Yao and Hensel from optical reflectivity experiments with normal incidence [2,3]. A prewetting transition, which is a first-order phase transition between a thin and a thick wetting film on the substrate, was evidenced from anomalous behaviors in the optical reflectivity. The prewetting transition line merges tangentially into the bulk liquid-vapor coexistence curve at the prewetting temperature $T_w = 1310\,^{\circ}\mathrm{C}$, and terminates at the prewetting critical point ($T_{pw}^{c} = 1468\,^{\circ}\mathrm{C}$ and $P_{pw}^{c} = 158.6$ MPa) lying close to the bulk critical point. The thickness of the wetting film was estimated on the assumption that the wetting film has a slab shape, and that the density and the optical constant of the slab are identical to those of liquid mercury at liquid-gas coexistence. For quantitative understanding of the physical properties of the wetting film, however, these assumptions should be checked more carefully.

Recently, it is found that not only optical reflectivity but also optical emissivity for the mercury-sapphire system show remarkable changes at the prewetting transition, and that the emissivity is more sensitive to the interfacial fluctuations than the optical reflectivity [4]. Indeed, in the prewetting supercritical phase, a sharp minimum in the emissivity is observed, and the anomaly is much stronger than that in the reflectivity. The strong anomaly in the emissivity is a clear indication of permittivity fluctuations in the wetting film associated with the prewetting critical phenomena.

Since the prewetting critical point (T_{pw}^{c}, P_{pw}^{c}) in this system lies very close to the bulk critical point (T_c, P_c) of fluid mercury, it is interesting to study how the bulk critical phenomena influence the surface critical phenomena. For example, competition between the wetting phenomena and the critical adsorption may be conceivable [5]. In addition, it is known that fluid mercury is transformed from metallic to nonmetallic under high temperature and pressure near the bulk critical point [6], and hence drastic changes in the adsorbate-substrate and adsorbate-adsorbate interactions should be caused by the metal-nonmetal (M-NM) transition. Thus the problem of how the wetting phenomena are influenced by the M-NM transition may be an intriguing subject of inquiry.

The purpose of the present paper is to study quantitatively the physical properties of the wetting film, such as the density (or the density profile), the thickness, and the coverage. For these purposes interface-sensitive measurements should be carried out. A simple extension of the normal reflection measurements may be an ellipsometric study with oblique incidence. In the conventional ellipsometry, the reflectivity ratio $\rho = r_p / r_s = \tan\psi \exp(i\delta)$ of p- and s-polarized light is measured. However, from the viewpoints of experimental technique, this method is not suitable for our experiments under high temperature and high pressure. The main problem is how to determine the phase shift δ, because δ is strongly affected by the birefringence of the sapphire window and the birefringence is highly temperature dependent. To our knowledge, sapphire is the only window material that is available up to the critical condition of mercury. Hence, we cannot use conventional ellipsometry in which the ellipsometric angles ψ and δ are detected.

In order to avoid these difficulties, we have developed a new method. Instead of ψ and δ, we have measured the

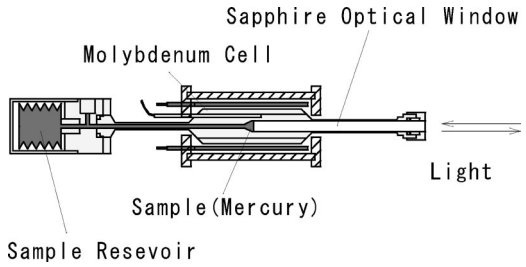

FIG. 1. Optical cell for reflectance measurements for mercury-sapphire interface.

intensity reflectances for *p*- and *s*-polarized lights, $R_p = |r_p|^2$ and $R_s = |r_s|^2$. In addition, we found that the sapphire window works as a polarizing prism by itself, and this enables us to measure R_p and R_s, separately. By using the reflectance data, we have studied the physical properties of the wetting film quantitatively. Preliminary results were given in previous papers [7,8]. In the present paper, full details of the experimental method, the observed data, and the results of analysis are described.

The paper is arranged as follows: In Sec. II, we describe the experimental methods, such as the principle of the reflectance measurements, layout of the optical system, and cell assembly. In Sec. III, experimental results are presented. These data are analyzed in Sec. IV. First, we estimate the optical constants of bulk fluid mercury in Sec. IV A. Then, by using these parameters, physical properties of the wetting film in the prewetting subcritical region are analyzed and discussed in Sec. IV B, and those in the prewetting supercritical region in Sec. IV C. Finally, a brief summary is given in Sec. V.

II. EXPERIMENT

We have performed optical reflectance measurements for a sapphire-mercury interface with normal reflection geometry and 45° reflection geometry. Figure 1 shows the cell assembly. The liquid sample was contained in a molybdenum cylindrical cell with an inner diameter of 6 mm. The cell was connected to a sample reservoir. The cell was closed at one end by a 95-mm long synthetic single-crystalline sapphire rod, which was used as an optical window. This cell assembly is similar to that used by Hensel and Yao [3].

In the normal reflection measurements, a sapphire rod that has a flat surface perpendicular to the axis of the rod was used, as shown schematically in the Fig. 2(a). In the 45° reflection measurements, on the other hand, we used a wedge shaped sapphire rod as shown in the Fig. 2(b). The axis of the rod was parallel to the optical axis (*c* axis) of the sapphire crystal, and the angle of the wedge was 90°. When the incident light comes along the axis of the rod, it is reflected successively by the two surfaces, and the reflected light goes back through the sapphire rod. It should be noted that, between the successive reflections, the *s*-polarized component propagates as the ordinary ray and the *p*-polarized component as the extraordinary ray. Therefore, the reflected *p*- and *s*-polarized lights split into two beams and go back in slightly different directions. This means that the wedge

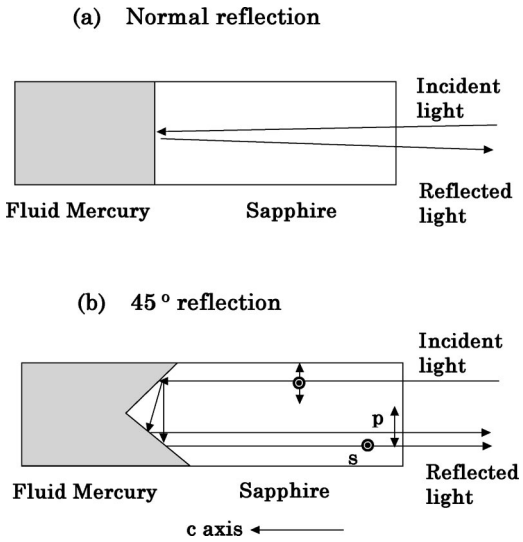

FIG. 2. Schematic illustrations of the optical paths through the sapphire rods for (a) the normal reflection measurements and (b) the 45° reflection measurements.

shaped sapphire rod works as a polarizing prism because of the birefringence of the sapphire crystal. Therefore, we can determine the reflectances for *p*- and *s*-polarized lights, R_p and R_s, separately by measuring the intensity of the two beams.

The cell was mounted inside an autoclave with a high-pressure window and an internal electric resistance furnace, as shown in Fig. 3. The autoclave was made of high-strength steel with 60 mm in inner diameter, 190 mm in outer diameter and 260 mm in axial length. The cylinder was closed by a 88 mm thick flange and a 93 mm thick flange. The furnace consists of two independently controlled heating elements made of molybdenum wire. The sample temperature was measured with two W-Re thermocouples in close contact with the hot part of the cell where the mercury sample was located. A high-pressure window in Fig. 3 was made of a sapphire with thickness of 19 mm and diameter of 15 mm. This window was supported by a flat area of a backup screw. Pure argon gas was used as pressure transmitting medium,

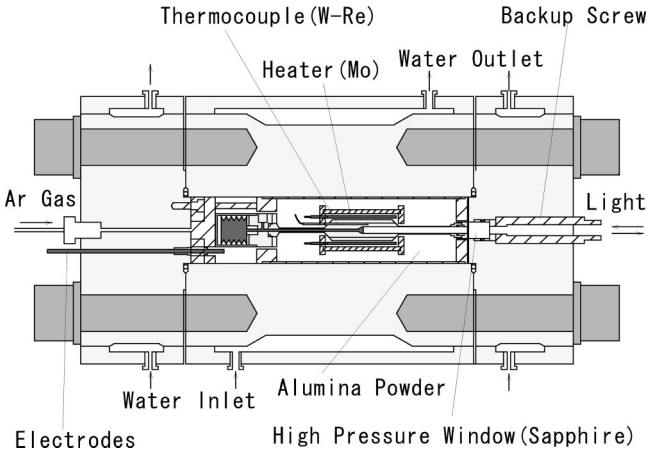

FIG. 3. Internally heated autoclave for reflectance measurements at high temperatures and pressures.

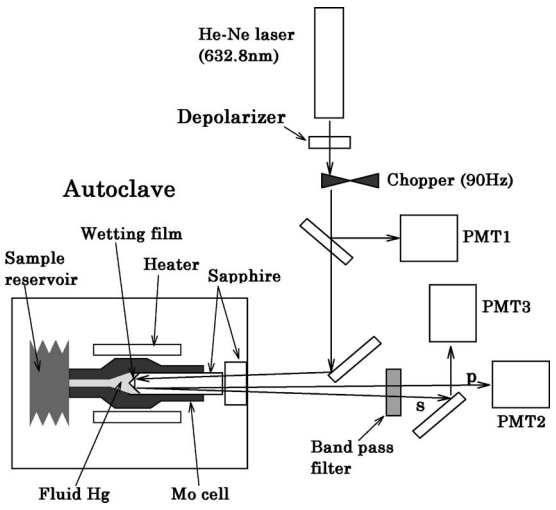

FIG. 4. The layout of the optical system for the 45° reflection measurements.

and the pressures of argon and fluid samples were balanced through the sample reservoir inside the autoclave. The pressure was measured using a Heise gauge with the accuracy of 0.3 MPa. The free volume in the autoclave was filled with alumina powder to obtain good thermal insulation and to prevent convection of the compressed argon gas. We calibrated the sample temperature by employing the most accurate vapor pressure data [9]. The vaporization temperature at a given pressure could easily be found as an abrupt change in the reflectances when the mercury sample is vaporized. The experimental error was less than 1 °C.

Figure 4 shows the layout of the optical system for the reflectance measurements with the 45° reflection geometry. A He-Ne laser (wavelength $\lambda = 632.8$ nm) was used as a light source. The light from the laser was depolarized and chopped at 90 Hz, and its intensity was monitored by a photomultiplier tube (PMT-1 in the figure). The reflected light was split into the *p* and *s* components due to the birefringence of the sapphire crystal, and both components were detected separately by two photomultiplier tubes (PMT-2 and PMT-3 in the figure). Before detection, the reflected light passed through a band-pass filter, which has a narrow transmission band around 632.8 nm, in order to suppress all spurious light such as thermal radiation. The background noise in the output signal of the PMT was eliminated by using a lock-in amplifier. For the lock-in detection, the output signal of PMT-1 was used as a reference signal.

In the 45° reflection measurements, the reflectances were calibrated by using the total reflection that occurs when the density of the bulk mercury vapor is smaller than 2.0 g/cm^3. For the normal reflection measurements, the reflectance was calibrated against the reflectance of the sapphire-mercury interface at the room temperature [10]. In the extreme conditions, an influence of Ar gas between the sapphire rod and the high-pressure sapphire window had to be taken into consideration, since the refractive index of Ar changes with pressure.

When the sapphire window is in direct contact with the bulk vapor or liquid phases of mercury (i.e., in the absence of the wetting film), the reflectance for the normal incidence (R_n), the reflectance for the *s*-polarized light (R_s), and the reflectance for the *p*-polarized light (R_p) in the 45° reflection geometry can be expressed in terms of the complex refractive index, $\tilde{n} = n + ik$, of bulk mercury [11]:

$$R_n = |r_n|^2 = \left| \frac{n_0 - \tilde{n}}{n_0 + \tilde{n}} \right|^2, \tag{2.1a}$$

$$R_s = |r_s|^2 = \left| \frac{n_0 - \sqrt{2\tilde{n}^2 - n_0^2}}{n_0 + \sqrt{2\tilde{n}^2 - n_0^2}} \right|^2, \tag{2.1b}$$

$$R_p = |r_p|^2 = \left| \frac{\tilde{n}^2 - n_0\sqrt{2\tilde{n}^2 - n_0^2}}{\tilde{n}^2 + n_0\sqrt{2\tilde{n}^2 - n_0^2}} \right|^2. \tag{2.1c}$$

Here $n_0 = 1.77$ is the refractive index of sapphire. It should be noted that, from equations (2.1b) and (2.1c), the relation

$$R_p = R_s^2 \tag{2.2}$$

always holds for the 45° reflection.

When the wetting film of mercury intrudes between the sapphire surface and the mercury vapor, R_n, R_s, and R_p change significantly, because the complex refractive index of the wetting film is much different from that of the mercury vapor. If the wetting film has a slab shape with a complex refractive index $\tilde{n}_{\mathrm{slab}} = n_{\mathrm{slab}} + ik_{\mathrm{slab}}$ and thickness l_{slab}, the reflectances R_i $(i = n,s,p)$ have the form [11]

$$R_i = \left| \frac{r_i^{01} + r_i^{12}\exp(2i\Delta)}{1 + r_i^{01} r_i^{12}\exp(2i\Delta)} \right|^2 \tag{2.3}$$

with

$$\Delta = \frac{2\pi l_{\mathrm{slab}}}{\lambda}\sqrt{\tilde{n}_{\mathrm{slab}}^2 - n_0^2 \sin^2\theta},$$

where r_i^{01} and r_i^{12} $(i = n,s,p)$ are the complex Fresnel reflection coefficients at the sapphire-wetting film interface, and at the wetting film-bulk vapor interface, respectively. The angle of reflection θ is 0 for $i = n$, and 45° for $i = s,p$.

It should be noted that, when the wetting film is present, relation (2.2) does not hold any more. For example, we have calculated how the R_p and R_s^2 depend on the film thickness l_{slab} in a typical case where the density of the wetting film is 7.0 g/cm^3 and the density of the coexisting vapor is 3.5 g/cm^3. Figure 5 shows the calculated R_p and R_s^2 as functions of l_{slab}. When l_{slab} increases, R_s^2 first decreases and then increases above 5 nm, while R_p increases monotonously. The ratio between R_p and R_s^2 changes by about an order of magnitude. Therefore we can detect the existence of the wetting film with high precision by comparing R_p and R_s^2.

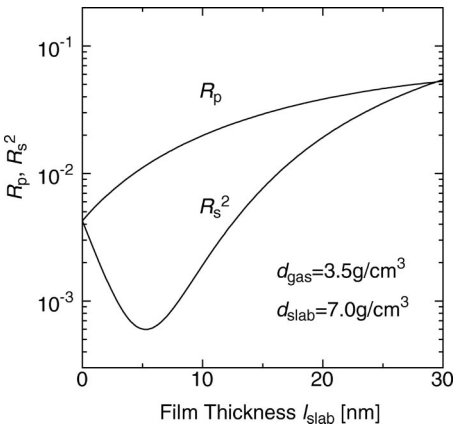

FIG. 5. Calculated reflectances for the *s*-polarized light (R_s) and for the *p*-polarized light (R_p) in the 45° reflection geometry in the case where a wetting film is present. They were calculated as functions of film thickness for a typical case where the density of the mercury wetting film is 7.0 g/cm^3 and the density of the coexisting vapor is 3.5 g/cm^3.

III. RESULTS

Representative results of the reflectance R_n in the normal reflection geometry are shown in Fig. 6, and those of R_p and R_s^2 in the 45° reflection geometry are shown in Fig. 7 as functions of pressure at various temperatures.

Figure 6(a) shows R_n in the normal reflection geometry at 1420 °C. When the pressure is decreased crossing the liquid-vapor coexistence line (indicated by ''LV'' in the figure), R_n jumps discontinuously. This jump is due to the difference between the optical constants of the liquid and vapor phases of mercury. In addition, R_n shows another discontinuous jump below the liquid-vapor coexistence (indicated by ''PW'' in the figure). This observation is completely consistent with that reported by Yao and Hensel [2,3], who attributed this reflectance anomaly to the prewetting transition.

The formation of the wetting film can be confirmed from the reflectance measurements in the 45° reflection geometry [7,8]. Figure 7(a) shows the pressure dependence of R_p (closed circles) and R_s^2 (open circles) in the 45° reflection geometry at 1328 °C. When the pressure is smaller than ~94 MPa, both R_p and R_s^2 shows a plateau, which implies that the refractive index n of mercury vapor is less than $n_0/\sqrt{2}$ in this region, and the total reflection occurs for the 45° reflection geometry. In this region, both R_p and R_s^2 are equal to unity, by which we can calibrate the reflectances. When the pressure is increased above 94 MPa, the reflectances decrease as the refractive index n of mercury vapor increase with density. In this region, R_p and R_s^2 coincide, implying that the wetting film does not exist on the sapphire surface, or it is too thin to be detected by this method. At 105.8 MPa (indicated by PW in the figure), R_s^2 shows a sudden decrease, while R_p does not show such a big change. The relation $R_p = R_s^2$ does not hold above this pressure, indicating that a thin film of mercury is formed on the sapphire-mercury interface, or the prewetting transition. When the pressure is increased further, R_p and R_s shows another jump, which corresponds

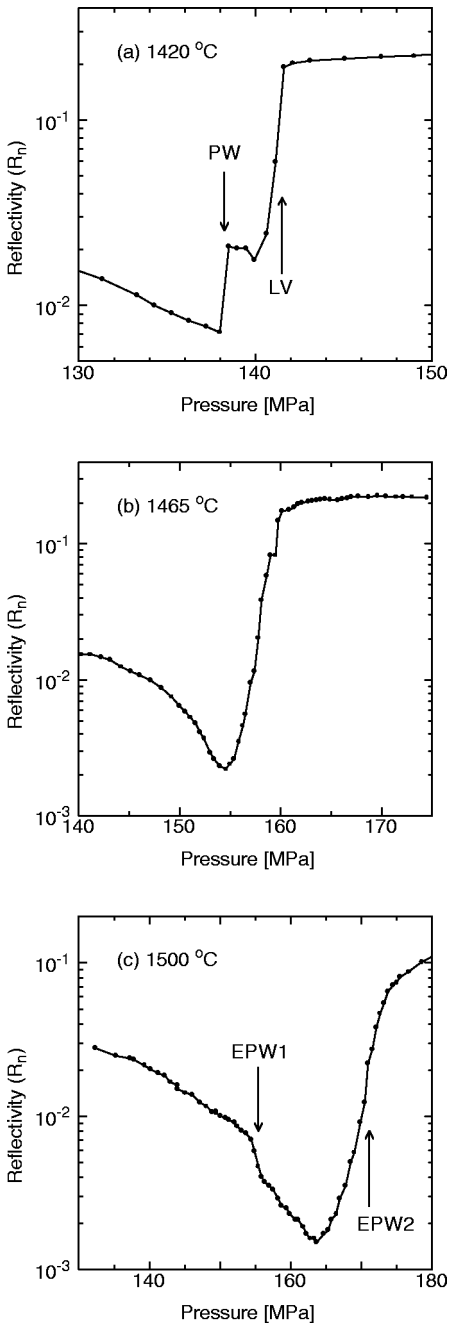

FIG. 6. Representative results of R_n in the normal reflection geometry, observed when the pressure is changed at the constant temperature of (a) 1420 °C, (b) 1465 °C, and (c) 1500 °C. PW and LV in (a) indicate the prewetting point and liquid-gas transition point, respectively. EPW1 and EPW2 in (c) indicate the anomalies observed in the prewetting-supercritical region.

to the vapor-liquid transition (indicated by LV in the figure). On the high-pressure side, where the bulk mercury is liquid, R_p and R_s^2 coincide again.

At higher temperatures, the wetting film below the prewetting pressure becomes noticeable. As an example, Fig. 7(b) shows the result at 1440 °C. When the pressure is increased up to the prewetting pressure (145 MPa), the difference between R_p and R_s^2 increases gradually, indicating that

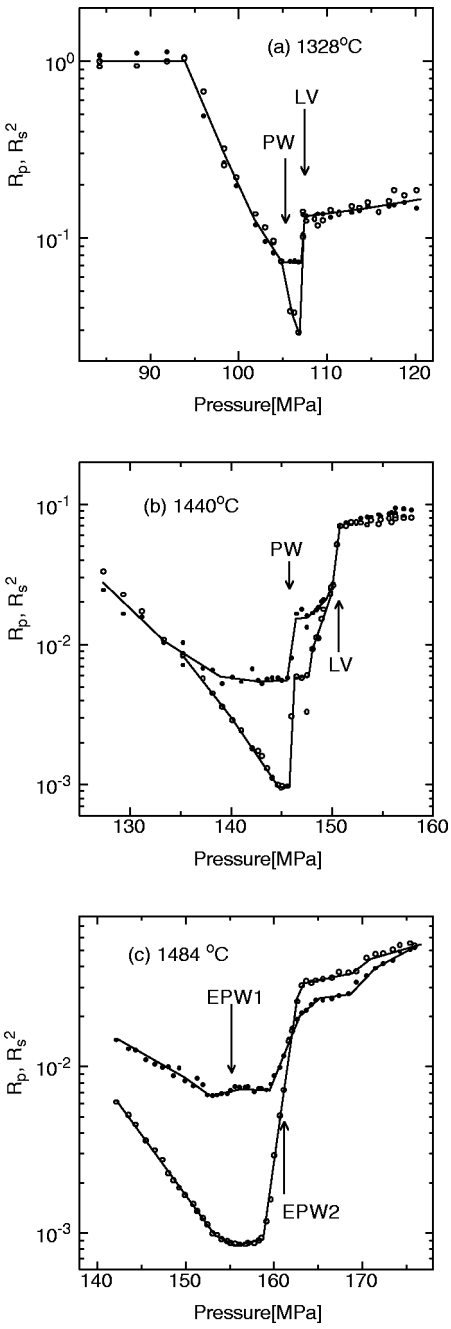

FIG. 7. Representative results of R_p (closed circles) and R_s^2 (open circles) in the 45° reflection geometry, observed when the pressure is changed at the constant temperature of (a) 1328 °C, (b) 1440 °C, and (c) 1484 °C. PW and LV in (a) and (b) indicate the prewetting point and liquid-gas transition point, respectively. EPW1 and EPW2 in (c) indicate the anomalies observed in the prewetting-supercritical region.

a thin mercury film is formed and grows on the sapphire substrate below the prewetting pressure.

When the temperature is increased further, the jump in the reflectances at the prewetting transition becomes smaller, and eventually it vanishes. As an example, Fig. 6(b) shows a result of R_n at 1465 °C. When the pressure is changed, R_n changes continuously, indicating that the change from thin to thick film is continuous in this region. This is in accordance

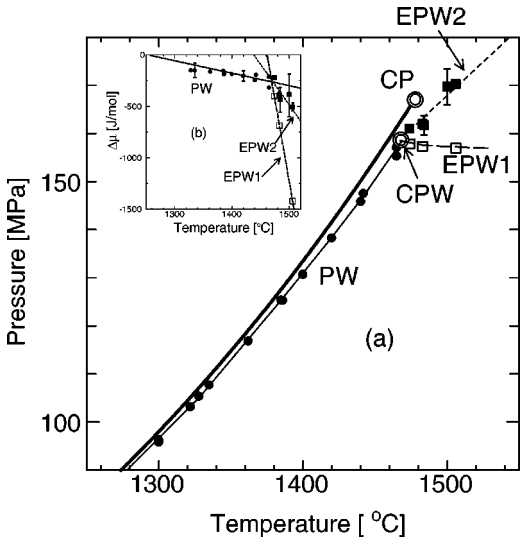

FIG. 8. The P-T phase diagram for mercury-sapphire system. The thick-solid line indicate the bulk liquid-vapor coexistence line. The solid circles show the state points where the reflectances exhibit discontinuous jumps. The solid and open squares show the anomalies in the reflectances above T_{pw}^c. The thin-solid line and dashed line indicate the prewetting line and its extension above T_{pw}^c, respectively. The inset shows the difference in chemical potential between the wetting film and the bulk liquid $\Delta\mu_{\text{jump}} = \mu_{\text{jump}} - \mu_o$ at the prewetting transition and its extension.

with the existence of the critical temperature T_{pw}^c of the prewetting transition [2,3].

In the prewetting supercritical one-phase region, two types of anomalies are observed in the reflectances albeit they are no longer discontinuous jumps. They are indicated by ''EPW1'' and ''EPW2'' in Fig. 6(c) showing R_n at 1500 °C, and in Fig. 7(c) showing R_p and R_s^2 at 1484 °C. One of the anomalies indicated by EPW1 appears as a kink in R_n around 155 MPa [Fig. 6(c)], and is less noticeable in R_p and R_s^2 [Fig. 7(c)]. The state points of EPW1 are plotted by the open squares on the P-T plane in Fig. 8 together with the prewetting line (PW) denoted by the solid line with solid circles. It should be noted that the EPW1 point coincides with the temperature and pressure where a sharp dip in the optical emissivity was observed [4]. The other anomaly indicated by EPW2 is characterized by a rapid but continuous increase in the reflectances. One might think that this is simply due to the increase in the density of bulk mercury. However, the state points of EPW2 are located at much lower pressures than the bulk saturated vapor pressure curve and its extension to the supercritical region. See also Fig. 8, where the EPW2 points are denoted by the closed squares above T_{pw}^c. Therefore, the secondary anomaly should also be assigned to an interfacial phenomenon. In Fig. 8, the loci of EPW1 and EPW2 may be regarded as extensions of the prewetting line, though both of them deviate towards lower pressures from the linear extrapolation of the PW. It is noticed that the line EPW2 nearly coincides with the isochore line of 4.0 g/cm^3 for the bulk fluid mercury.

The inset in the Fig. 8 shows the difference in chemical potential between the wetting film and the bulk liquid at the

prewetting transition, $\Delta\mu_{\rm jump}=\mu_{\rm jump}-\mu_o$. The wetting temperature T_w can be estimated by extrapolating the values of $\Delta\mu_{\rm jump}$ to the coexistence curve, represented by the horizontal line $\Delta\mu_{\rm jump}=0$. If we adopt a simple linear extrapolation, the wetting temperature T_w is estimated to be about 1260 $\pm 20\,^\circ$C, which is slightly lower than that estimated by Yao and Hensel (1310 °C) [2,3]. If the prewetting line curves and merges tangentially into the liquid-gas coexistence line, as predicted theoretically [12], T_w takes a lower value. However, it must be pointed out that in practice it is very difficult to determine T_w precisely, because the prewetting transition line and the liquid-gas coexistence line become hard to distinguish experimentally at a temperature smaller than 1330 °C.

The critical temperature and pressure of prewetting, T_{pw}^c and P_{pw}^c, are estimated from the crossing point of the three lines PW, EPW1, and EPW2 in the inset of the Fig. 8. In the present paper, they are estimated to be $T_{pw}^c=1470\pm 3\,^\circ$C and $P_{pw}^c=158.5\pm 1$ MPa, which nicely agree with those reported by Yao and Hensel [2,3].

IV. ANALYSIS AND DISCUSSION

A. Bulk refractive index

First, we have estimated the complex refractive index $\tilde{n}=n+ik$ of bulk fluid mercury. In the present paper, we assumed that $\tilde{n}$ depends only on density d and not on temperature T. This is because the most relevant parameter determining various properties of fluid mercury around the critical region is the density [6]. $\tilde{n}$ was calculated from the reflectance data far from the liquid-vapor coexistence curve, where no wetting film is present. For this calculation, we used not only the 45° reflection data, R_p and R_s, but also the normal reflection data R_n, because R_p and R_s are not independent as stated in Sec. II (the relation (2.2) always holds for the bulk sample in the 45° reflection geometry) and we need two independent reflectance data to derive two unknown parameters n and k.

Figure 9(a) shows the observed reflectances R_n, R_s, and R_p. Below $d=2.0$ g/cm^3, R_s, and R_p are equal to unity due to the total reflection. Around $d=3.8$ g/cm^3, the reflectances are very small because n is close to n_0.

In principle, one could deduce n and k from the combination of R_n and R_s (or R_p) at each density d. However, this would give n and k, which could suffer significantly from experimental errors in individual data. Hence, we will describe n and k as smooth functions of d[$n(d)$ and $k(d)$] that satisfy the following requirements:

(1) In the low-density region below $d_1=2.0$ g/cm^3, $n(d)$ should have the form of the Lorentz-Lorenz formula with a parameter α, which is proportional to the polarizability of an isolated atom. When the density is increased, n deviates upward from the Lorentz-Lorenz formula.

(2) In the low-density region below $d_2=5.0$ g/cm^3, k should be zero, because the absorption coefficient for the light with the wavelength $\lambda=632.8$ nm is nearly zero below

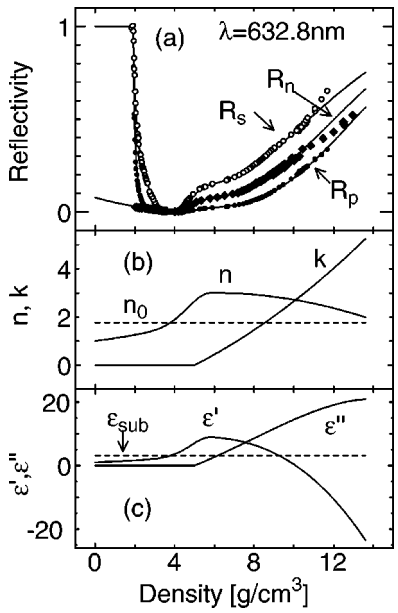

FIG. 9. (a) The density dependence of the reflectances of bulk fluid mercury against the sapphire window for the light with wavelength $\lambda=632.8$ nm. The solid diamonds are reflectance for the normal incidence (R_n), the open circles and closed circles are reflectance for the *s*-polarized light (R_s) and for the *p*-polarized light (R_p) in the 45° reflection geometry, respectively. The solid lines are the reflectances calculated from n and k shown in (b). (b) The optical constants n and k of bulk mercury, estimated from the reflectance data of (a) as functions of density. (c) The real and the imaginary parts of the dielectric function $\tilde{\epsilon}=\tilde{n}^2=\epsilon'+i\epsilon''$. The dashed lines in (b) and (c) indicate the refractive index n_0 and the dielectric function $\epsilon_{\rm sub}$ of the sapphire substrate, respectively.

5.0 g/cm^3 [13]. Above d_2, k should increase monotonously with d.

(3) At the density $d=13.6$ g/cm^3, n, and k should coincide with the values of reference [10], which were measured under the ambient condition.

At the intermediate densities, n and k should exhibit nontrivial behavior. In the present paper, we have employed the following trial functions for $n(d)$ and $k(d)$:

$$n(d)=\begin{cases}\sqrt{\dfrac{1+2\alpha d}{1-\alpha d}}+g(d) & (0\leqslant d\leqslant d_1=2.0\ \text{g/cm}^3)\\ n_1+n_2(d-d_1)+n_3(d-d_1)^2+g(d) & (d_1<d\leqslant 13.6\ \text{g/cm}^3),\end{cases} \tag{4.1}$$

$$k(d)=\begin{cases}0 & (0\leqslant d\leqslant d_2=5.0\ \text{g/cm}^3)\\ k_1(d-d_2)+k_2(d-d_2)^2 & (d_2<d\leqslant 13.6\ \text{g/cm}^3),\end{cases} \tag{4.2}$$

where

$$g(d)=\begin{cases}A\exp\{-[(d-d_0)/\sigma_1]^2\} & (d\leqslant d_0)\\ A\exp\{-[(d-d_0)/\sigma_2]^2\} & (d_0\leqslant d)\end{cases}$$

TABLE I. Parameters that describe the density dependence of the bulk optical constants $n(d)$ and $k(d)$. [See Eqs. (4.1) and (4.2).] The parameters without asterisk (*) were determined from the fitting and the parameters with asterisk (*) were calculated from other parameters.

α (cm^3/g)	n_1^*	n_2^* (cm^3/g)	n_3^* (cm^6/g^2)	A	d_0 (g/cm^3)	σ_1 (g/cm^3)	σ_2 (g/cm^3)	k_1 (cm^3/g)	k_2^* (cm^6/g^2)
7.9×10^{-2}	1.25	0.105	-1.46×10^{-2}	1.49	5.85	1.68	2.54×10^{2}	0.420	2.20×10^{-2}

is a nonsymmetric Gaussian function. The introduction of $g(d)$ is useful to reproduce the behavior of $n(d)$ around an intermediate density d_0, which is treated as a free parameter. The parameters n_1 and n_2 are determined from the condition that $n(d)$ and its derivative are continuous at d_1, and n_3 and k_2 are from the condition that n and k should be fixed to 1.99 and 5.24, respectively, at $d=13.6$ g/cm^3 [10]. Therefore, $n(d)$ and $k(d)$ are expressed by six free parameters α, A, d_0, σ_1, σ_2, and k_1. These free parameters were adjusted to fit the calculated reflectances to the observed ones. The obtained parameters are listed in Table I. It is noticed that σ_2 converged to a very large value (2.54×10^2 g/cm^3) compared to $d-d_0$, and the nonsymmetric Gaussian function $g(d)$ is nearly constant ($g(d)\simeq A$) in the region $d>d_0$.

Figure 9(b) shows the estimated $n(d)$ and $k(d)$. These $n(d)$ and $k(d)$ reproduce density dependencies of R_n, R_s, and R_p very well as shown by solid lines in Fig. 9(a). Figure 9(c) shows the real and the imaginary parts of the dielectric function $\tilde{\epsilon}=\tilde{n}^2=\epsilon'+i\epsilon''$ for the light with wavelength $\lambda=632.8$ nm. The overall feature of the ϵ' is similar to that reported previously [14]. The cusplike behavior of the ϵ' around $d=d_0=5.85$ g/cm^3 is consistent with a theoretical prediction of a dielectric anomaly [15], which is expected to occur at the density smaller than the metal-nonmetal transition for the finite frequency ω.

B. Wetting film in the prewetting subcritical region

Next, physical properties of the wetting film are elucidated from the observed reflectance data, $R_p^{\rm obs}$ and $R_s^{\rm obs}$. The main interest in the present paper is the density profile $d_l(z)$ and the coverage Γ of the wetting film. Here z is the coordinate normal to the surface and $z=0$ is defined as the surface of the sapphire substrate. The coverage Γ is defined by

$$\Gamma=\int_0^\infty dz[d_l(z)-d_{\rm gas}], \tag{4.3}$$

where $d_{\rm gas}$ is the density of the coexisting bulk vapor phase.

As a first approximation, we assume that the wetting film has a slab shape as shown in Fig. 10(a). In the slab model, the density profile $d_l^{\rm slab}(z)$ has a constant value $d_{\rm slab}$ for $z<l_{\rm slab}$, where $l_{\rm slab}$ is the thickness of the film, and jumps abruptly to the density of the coexisting bulk vapor phase, $d_{\rm gas}$, and hence the coverage Γ is expressed simply as $(d_{\rm slab}-d_{\rm gas})l_{\rm slab}$. In addition, we make an assumption that the optical constant of the wetting film is a function of the density $d_{\rm slab}$ of the film, i.e., $\tilde{n}_{\rm slab}(d_{\rm slab})=n_{\rm slab}(d_{\rm slab})+ik_{\rm slab}(d_{\rm slab})$, and has the same functional form as that for the bulk phase [see Fig. 9(b)]. Note that the density $d_{\rm slab}$ is not necessarily equal to that of the bulk liquid phase, $d_{\rm liq}$.

Within the framework of the slab model, the reflectances R_p and R_s can be easily calculated from $\tilde{n}_{\rm slab}(d_{\rm slab})$ and $l_{\rm slab}$ by using Eq. (2.3). Inversely, $d_{\rm slab}$ and $l_{\rm slab}$ are calculated from the reflectance data by minimizing the discrepancy factor D defined by

$$D=[\log(R_p^{\rm obs})-\log(R_p^{\rm cal})]^2+[\log(R_s^{\rm obs})-\log(R_s^{\rm cal})]^2,$$

where $R_i^{\rm obs}$ and $R_i^{\rm cal}$ $(i=p,s)$ are the observed and calculated reflectances, respectively. As an example, Fig. 11 shows a contour map of D on the $(d_{\rm slab},l_{\rm slab})$ plane for the observed data at $P=146.3$ MPa and $T=1440\,^\circ$C, where $R_p^{\rm obs}=0.0149$, $R_s^{\rm obs}=0.0539$, and the density of the coexisting

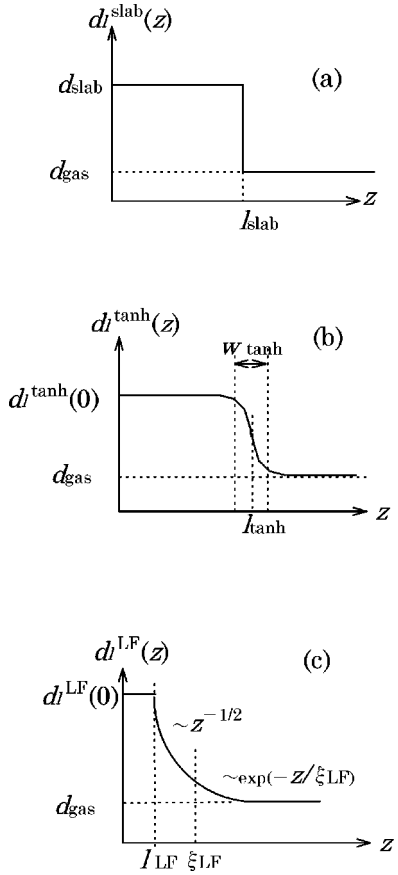

FIG. 10. Density profile models for the wetting film used in the present paper. (a) indicates the slab model and (b) the slowly varying tanh profile [see Eq. (4.5)] and (c) the power-law exponential type profile [see Eqs. (4.6a) and (4.6b)].

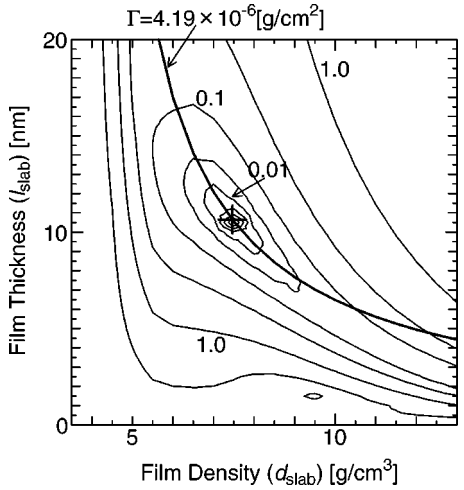

FIG. 11. A contour map of the discrepancy factor D on the $(d_{\mathrm{slab}},l_{\mathrm{slab}})$ plane. D was calculated for the observed data at $P=146.3$ MPa and $T=1440\,^{\circ}\mathrm{C}$, where $R_p^{\mathrm{obs}}=0.0149$, $R_s^{\mathrm{obs}}=0.0539$, and the density of the coexisting vapor is 3.53 g/cm^3. The cross indicates the point $(d_{\mathrm{slab}},l_{\mathrm{slab}})$ which minimizes D. The thick-solid line indicates $\Gamma=4.19\times10^{-6}$ g/cm^2=const.

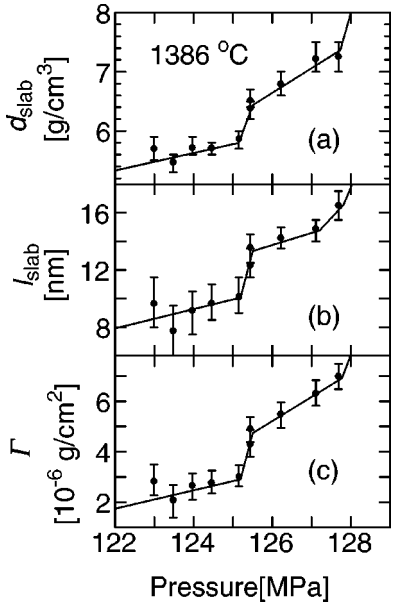

FIG. 12. The density d_{slab} (a), the thickness l_{slab} (b), and the coverage Γ (c) of the wetting film estimated from the reflectance data R_p and R_s at 1386 °C by using the slab model.

vapor is 3.53 g/cm^3. The point $(d_{\mathrm{slab}},l_{\mathrm{slab}})$ which minimizes D, is indicated by a cross in the figure. It is noticed that, except for the near vicinity of the minimum, the contours are not round but elongated, forming a ''valley.'' Since R_p^{obs} and R_s^{obs} contain experimental errors, the true values of d_{slab} and l_{slab} could deviate from the apparent minimum of D, but they should still remain in the valley as long as the errors are not significant. Thus the uncertainties of d_{slab} and l_{slab} can be estimated from the extent of the valley. In contrast, the coverage $\Gamma=(d_{\mathrm{slab}}-d_{\mathrm{gas}})l_{\mathrm{slab}}$ proves to have smaller uncertainties and it is much more reliable than the individual parameters d_{slab} and l_{slab}, because the uncertainties of the d_{slab} and l_{slab} are canceled out due to their negative correlation. This is easily understood from the Fig. 11. The line $\Gamma=4.19\times10^{-6}$ g/cm^2=const, which is indicated by a thick solid line, lies along the valley, and the uncertainties of the individual parameters d_{slab} and l_{slab} does not affect the value of Γ significantly.

Figure 12 shows the parameters d_{slab}, l_{slab}, and Γ calculated from the reflectance data R_p and R_s at 1386 °C. When the pressure is increased across the prewetting transition ($\sim$125.3 MPa), discontinuous jumps in these parameters are observed clearly. Below the prewetting transition, d_{slab}, l_{slab}, and Γ are estimated to be 5.9 ± 0.2 g/cm^3, 10.0 ± 1.0 nm, and $3.0\pm0.5\times10^{-6}$ g/cm^2, respectively. Above the prewetting transition, d_{slab}, l_{slab}, and Γ jump discontinuously to 6.5 ± 0.2 g/cm^3, 13.5 ± 1.0 nm, and $4.9\pm0.5\times10^{-6}$ g/cm^2, respectively.

Above the prewetting transition, the present film thickness is in the same order as that obtained by Yao and Hensel [2,3]. For example, at 1400 °C, Yao and Hensel estimated the film thickness at $\sim$9.5 nm. This value is slightly smaller than ours, probably because they assumed the density of the wetting film to be the same as liquid mercury at liquid-gas coexistence. Although their individual parameters l_{slab} and d_{slab} are slightly different from ours, the coverage Γ is nearly equal to ours ($\sim5\times10^{-6}$ g/cm^2) around this temperature and pressure region. Below the prewetting transition, on the other hand, the present film thickness is much larger than that obtained by Yao and Hensel. This may be because the present 45° reflection technique is much more sensitive to the thin wetting film than the normal reflection measurements.

Figure 13 shows the density of the wetting film d_{slab} at the prewetting transition, together with the density of the bulk fluid mercury at the liquid-gas coexistence. It should be noted that the d_{slab} is much smaller than the density of the bulk liquid phase d_{liq} at the liquid-vapor coexistence curve. A possible interpretation for this result is that the sapphire substrate prefers wetting film with lower density. This interpretation may be derived from the theory of long-range dis-

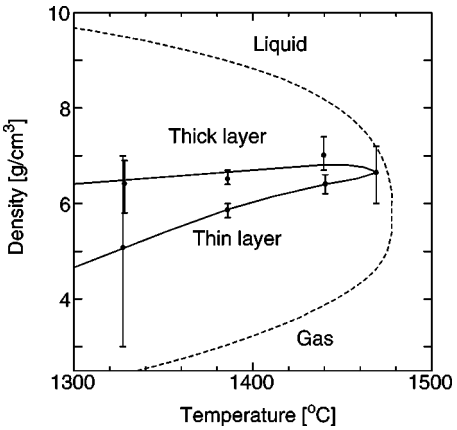

FIG. 13. The density of the wetting film at the prewetting transition. The dashed line indicate the density of the bulk fluid mercury at the liquid-gas coexistence.

persion forces between polarizable media (Lifshitz theory) [16]. When the thickness l_{slab} of the wetting film is small enough and the retardation effect can be neglected, the van der Waals chemical potential is deduced from the general formula given by Dzyaloshinsky *et al.* [17]:

$$\mu = -\frac{\hbar}{16\pi^2 \rho l_{\mathrm{slab}}^3}\int_0^\infty d\omega \int_0^\infty dx x^2 [f(i\omega)^{-1} e^x + 1]^{-1}$$

$$\simeq -\frac{\hbar}{8\pi^2 \rho l_{\mathrm{slab}}^3}\int_0^\infty d\omega f(i\omega), \tag{4.4}$$

where

$$f(i\omega) = \frac{\epsilon_{\mathrm{sub}}(i\omega) - \epsilon_{\mathrm{slab}}(i\omega)}{\epsilon_{\mathrm{sub}}(i\omega) + \epsilon_{\mathrm{slab}}(i\omega)} \frac{\epsilon_{\mathrm{slab}}(i\omega) - \epsilon_{\mathrm{gas}}(i\omega)}{\epsilon_{\mathrm{slab}}(i\omega) + \epsilon_{\mathrm{gas}}(i\omega)}$$

and ρ is the number density of mercury atoms in the wetting film. $\epsilon_{\mathrm{sub}}(i\omega)$, $\epsilon_{\mathrm{slab}}(i\omega)$, and $\epsilon_{\mathrm{gas}}(i\omega)$ are dielectric functions for the sapphire substrate, the wetting film, and the coexisting mercury gas phase, respectively, at imaginary frequencies $i\omega$. $\epsilon(i\omega)$ is calculated from the imaginary part of the dielectric function $\epsilon''(\omega)$ by using the relation

$$\epsilon(i\omega) = 1 + \frac{2}{\pi}\int_0^\infty d\omega' \frac{\omega' \epsilon''(\omega')}{\omega'^2 + \omega^2}.$$

It is known that the dielectric function of fluid mercury changes dramatically with density [6]. When the density is higher than 9 g/cm^3, fluid mercury has a metallic nature, and the dielectric function diverges at $\omega = 0$. Therefore, when d_{slab} is greater than 9 g/cm^3 and the wetting film has metallic nature, $\epsilon_{\mathrm{slab}}(i\omega) > \epsilon_{\mathrm{sub}}(i\omega)$, $\epsilon_{\mathrm{slab}}(i\omega) > \epsilon_{\mathrm{gas}}(i\omega)$ at low frequencies, and hence μ is positive, leading to nonwetting. When the density is decreased below 9 g/cm^3, on the other hand, the properties of fluid mercury change to nonmetallic with a finite-energy gap, which implies the dielectric function has a finite value at $\omega = 0$. Accompanied by the metal-nonmetal transition, $\epsilon_{\mathrm{slab}}(i\omega)$ decreases and becomes smaller than $\epsilon_{\mathrm{sub}}(i\omega)$ in a wide range of the frequency ω [$\epsilon_{\mathrm{slab}}(i\omega) < \epsilon_{\mathrm{sub}}(i\omega)$, $\epsilon_{\mathrm{slab}}(i\omega) > \epsilon_{\mathrm{gas}}(i\omega)$]. Therefore, μ is expected to decrease with decreasing d_{slab}. Our preliminary calculation of μ by using the dielectric function at various densities [18] shows that μ changes its sign from positive to negative when the density d_{slab} is decreased below ~8 g/cm^3, and it is expected that μ decreases as d_{slab} decreases further. This may be a reason why the sapphire substrate prefers wetting film with lower density d_{slab} than that of the coexisting bulk liquid d_{liq}.

When the pressure approaches the liquid-gas coexistence, the wetting film is expected to grow into a macroscopic liquid film, namely, d_{slab} is expected to approach d_{liq}, and l_{slab} and Γ are expected to diverge. However, at high temperatures close to T_{pw}^c, the observation was different from this expectation. As an example, the solid circles in Fig. 14 show the parameters d_{slab}, l_{slab}, and Γ at 1440 °C obtained by using the slab model. When the pressure approaches the liquid-gas coexistence, d_{slab} does not approach d_{liq}, and even

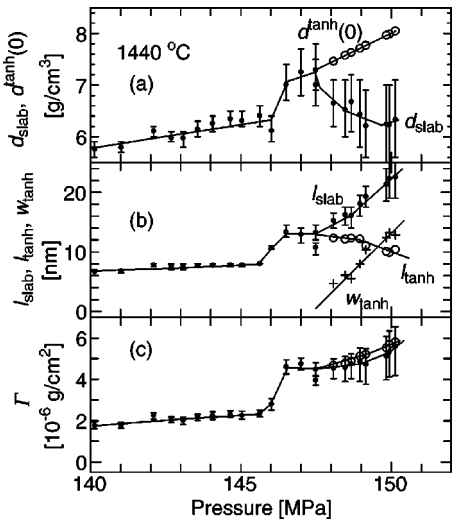

FIG. 14. The solid circles indicate the density d_{slab} (a), the thickness l_{slab} (b), and the coverage Γ (c) of the wetting film estimated from the reflectance data R_p and R_s at 1440 °C [Fig. 7(b)] by using the slab model. The open circles in (a), the open circles in (b), the crosses in (b), and the open circles in (c) indicate the estimated parameters for the tanh-profile model, $d_l^{\mathrm{tanh}}(0)$, l_{tanh}, w_{tanh}, and Γ, respectively [see Eq. (4.5)]. In the present paper, $d_l^{\mathrm{tanh}}(0)$ was fixed to the linear interpolation between $d_{\mathrm{liq}} = 8.16$ g/cm^3 at $P = 150$ MPa (liquid-gas transition pressure), and $d_{\mathrm{slab}} = 7.30$ g/cm^3 at $P = 147$ MPa.

shows a sharp decrease. This result could partly be explained from the above-mentioned theory that the sapphire substrate prefers a wetting film with lower density. Another possible explanation is that the slab model is not sufficient to describe the shape of the wetting film, and a smooth variation of the density $d_l(z)$ as a function of coordinate z has to be taken into account. This smooth density profile may be due to the broadening of the liquid-gas interface, or may be the result of lateral fluctuation at the liquid-gas interface. The former mechanism is expected to become important near the bulk liquid-vapor critical point where the correlation length becomes large, and the latter is expected to become important near the liquid-gas coexistence curve or near the prewetting curve (including its extension to the prewetting supercritical region), where the two-dimensional compressibility diverges and interfacial fluctuations play a major role.

In order to test the influence of the smooth density profile on the reflectances, we assume that $d_l(z)$ has the following tangent-hyperbolic (tanh) form:

$$d_l^{\mathrm{tanh}}(z) = \frac{1}{2}[d_l^{\mathrm{tanh}}(0) - d_{\mathrm{gas}}][1 + \exp(-2l_{\mathrm{tanh}}/w_{\mathrm{tanh}})] \times \{1 + \tanh[-(z - l_{\mathrm{tanh}})/w_{\mathrm{tanh}}]\} + d_{\mathrm{gas}}, \tag{4.5}$$

where l_{tanh} and w_{tanh} are parameters characterizing the thickness of the film and broadness of the liquid-gas interface, respectively. A schematic illustration of this density profile is shown in Fig. 10(b). We also assume that the refractive index $\tilde{n}(z)$ at each z is determined from the $d_l^{\mathrm{tanh}}(z)$ by using the function shown in the Fig. 9(b). Then, R_p^{cal} and R_s^{cal} were

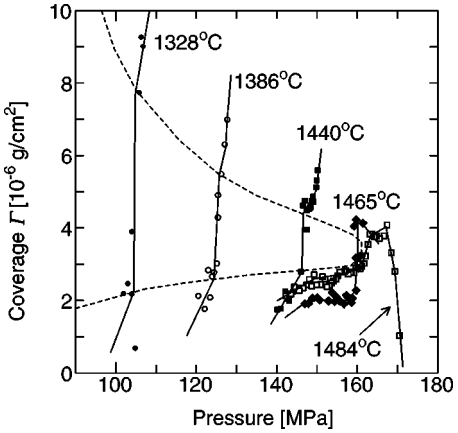

FIG. 15. Pressure variation of the coverage Γ at several temperatures. The closed circles: 1328 °C, the open circles: 1386 °C, the closed squares: 1440 °C, the closed diamonds: 1465 °C, and the open squares: 1484 °C.

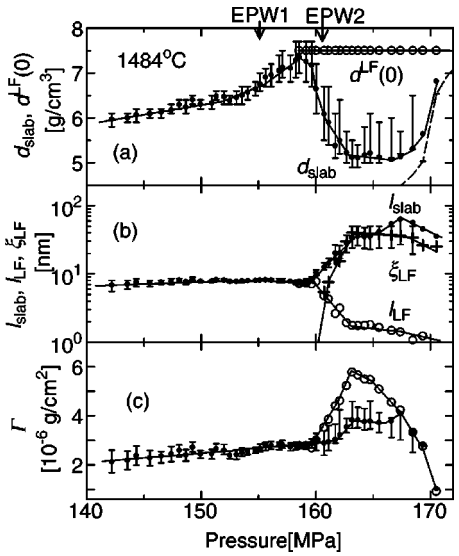

FIG. 16. The solid circles indicate the density d_{slab} (a), the thickness l_{slab} (b), and the coverage Γ (c) of the wetting film estimated from the reflectance data R_p and R_s at 1484 °C [Fig. 7(c)] by using the slab model. The open circles in (a), the open circles in (b), the crosses in (b), and the open circles in (c) indicate the estimated parameters for the slowly varying power-law exponential type profile, $d_l^{\mathrm{LF}}(0)$, l_{LF}, ξ_{LF}, and Γ, respectively [see Eqs. (4.6a) and (4.6b)]. In the present paper, $d_l^{\mathrm{LF}}(0)$ was fixed to 7.5 g/cm^3. The dashed line in (a) is the density of the bulk fluid mercury.

calculated by solving Maxwell's equation numerically (see the Appendix), and free parameters l_{tanh} and w_{tanh} were optimized by minimizing the discrepancy factor D. In this calculation, the density $d_l^{\mathrm{tanh}}(0)$ at $z=0$ has to be fixed, because we can determine only two free parameters from the two independent data, R_p^{obs} and R_s^{obs}. In the present paper, $d_l^{\mathrm{tanh}}(0)$ was fixed to the linear interpolation between $d_{\mathrm{liq}}=8.16$ g/cm^3 at $P=150$ MPa (liquid-gas transition pressure), and $d_{\mathrm{slab}}=7.30$ g/cm^3 at $P=147$ MPa, as indicated by open circles in Fig. 14(a).

The open circles and the crosses in Fig. 14(b) indicate the estimated values of l_{tanh} and w_{tanh}, respectively. When the pressure approaches the liquid-gas coexistence, w_{tanh} increases and becomes comparable to l_{tanh}, indicating broadening of the liquid-vapor interface in the tanh model. The broadening of the interface is compatible with the observation of thermal radiation that the interfacial fluctuations increase near the liquid-gas coexistence [4]. It is also consistent with the apparent sharp decrease of d_{slab} in the slab model [see the solid circles in Fig. 14(a)].

Comparison of the coverage Γ is made between the tanh model (denoted by the open circles) and the slab model (denoted by the solid circles) in Fig. 14(c). It is noticed that Γ does not significantly depend on the model. This means that Γ is more reliable as an order parameter than individual parameters such as d_{slab}, l_{slab}, etc., which are strongly model-dependent quantities.

Figure 15 shows the pressure variation of the coverage Γ at several temperatures. The isotherms at $T<1470$ °C show a jump in Γ at the prewetting line. When the temperature increases, the jump decreases and vanishes above the prewetting critical temperature.

C. Wetting film in the prewetting supercritical region

In the prewetting supercritical region, two types of anomalies were observed in the reflectivity. The line EPW1 in Fig. 8 is characterized by the small kink in R_n [Fig. 6(c)]. At the same temperatures and pressures, a substantial reduction of the optical emissivity was observed owing to the interfacial fluctuations [4]. Hence the anomaly EPW1 can be identified as an increase of the interfacial fluctuation in the wetting film [4]. The kink observed in R_n may be attributed to the reduction of the reflectance induced by the fluctuation in the wetting film. On the other hand, the line EPW2 is characterized by the rapid but not discontinuous increase in the reflectances [Figs. 6(c) and 7(c)]. We believe that the lateral fluctuations play a minor role at the anomaly EPW2, because the optical emissivity does not change strongly.

In order to investigate the detail of these anomalies, we calculated the density profile from the reflectance data R_p and R_s at 1484 °C [Fig. 7(c)], which is above the liquid-vapor critical point $T_c=1478$ °C. As a first approximation, we have applied the slab model to analyze the reflectance data. The solid circles in Fig. 16 show the parameters d_{slab}, l_{slab}, and Γ obtained by using the slab model. At the pressure corresponding to EPW1, the parameters do not show strong anomalies, because the changes in R_p and R_s^2 are very small. When the pressure is increased above EPW2, on the other hand, d_{slab} shows a sharp decrease, and l_{slab} and Γ show a rapid increase. This behavior is similar to that observed at 1440 °C near the liquid-gas transition [Fig. 14(a)] but more prominent, and it may be interpreted as the result of broadening of the density profile $d_l(z)$. This interpretation is consistent with the fact that the correlation length of the bulk fluid phase becomes large near the liquid-vapor critical point.

In order to analyze the density profile near the critical point, we have tentatively used the tanh-type density profile model, i.e., Eq. (4.5), and found that l_{slab} converged to negative values above the line EPW2. The negative l_{slab} means that the density profile has no plateau, and declines very steeply with increasing z. This result indicates that it is not

necessary to use the tanh model. Then, alternatively, we adopt a power-law exponential type adsorption profile, proposed by Liu and Fisher [19],

$$d_l^{\mathrm{LF}}(z)=P_0 t^{\beta}\left(\frac{1+cz/\xi_{\mathrm{LF}}}{z/\xi_{\mathrm{LF}}}\right)^{\beta/\nu} e^{-z/\xi_{\mathrm{LF}}}+d_{\mathrm{gas}}.$$

Here, t is the reduced temperature $t=(T-T_c)/T_c$ and ξ_{LF} is the correlation length. As usual, β and ν describe the critical behavior of the coexistence curve and the correlation length ξ_{LF}. The function $d_l^{\mathrm{LF}}(z)-d_{\mathrm{gas}}$ varies as $(z/\xi_{\mathrm{LF}})^{\beta/\nu}$ for small z/ξ_{LF} and as $e^{-z/\xi_{\mathrm{LF}}}$ for large z/ξ_{LF}. This density profile satisfies the scaling law proposed by Fisher and de Gennes [20]. The theoretical estimates of the exponents for the three-dimensional Ising model, $\beta=0.328\pm0.004$ and $\nu=0.632\pm0.001$, yield $\beta/\nu=0.519\pm0.007$ [21]. Following Liu and Fisher [19], we adopted the approximation $\beta/\nu=1/2$ in place of 0.519 in the present paper. The parameter c, which tunes the crossover from algebraic to exponential decay, is expected to be of order unity [19]. In the present paper, we adopted $c=1$ for simplicity. In order to suppress the divergence of the density in the small-z region, we introduced a cutoff density $d_l^{\mathrm{LF}}(0)$ for z smaller than a cutoff distance l_{LF}. Then, the density profile $d_l^{\mathrm{LF}}(z)$ is simplified as

$$d_l^{\mathrm{LF}}(z)=[d_l^{\mathrm{LF}}(0)-d_{\mathrm{gas}}]\left(\frac{(\xi_{\mathrm{LF}}+z)l_{\mathrm{LF}}}{(\xi_{\mathrm{LF}}+l_{\mathrm{LF}})z}\right)^{1/2} \times\exp[-(z-l_{\mathrm{LF}})/\xi_{\mathrm{LF}}]+d_{\mathrm{gas}} \tag{4.6a}$$

for $z>l_{\mathrm{LF}}$, and

$$d_l^{\mathrm{LF}}(z)=d_l^{\mathrm{LF}}(0) \tag{4.6b}$$

for $z<l_{\mathrm{LF}}$. A schematic illustration of this density profile is shown in Fig. 10(c). It should be noted that, when $\xi_{\mathrm{LF}}\ll l_{\mathrm{LF}}$, the density profile $d_l^{\mathrm{LF}}(z)$ coincides with that of the slab model $d_l^{\mathrm{slab}}(z)$ with $l_{\mathrm{slab}}=l_{\mathrm{LF}}$ and $d_{\mathrm{slab}}=d_l^{\mathrm{LF}}(0)$. R_p^{cal} and R_s^{cal} can be calculated from this model profile by solving Maxwell's equation numerically, and the free parameters l_{LF} and ξ_{LF} are optimized by minimizing the discrepancy factor D. In this calculation, the density $d_l^{\mathrm{LF}}(0)$ at $z=0$ has to be fixed, because we can determine only two free parameters from the two independent data, R_p^{obs} and R_s^{obs}. This procedure is identical to that for the tanh model. In the present paper, $d_l^{\mathrm{LF}}(0)$ was fixed to 7.5 g/cm^3, which is near the maximum of the d_{slab}. The $d_l^{\mathrm{LF}}(0)$ is indicated by open circles in Fig. 16(a).

The open circles and the crosses in Fig. 16(b) indicate the estimated parameters l_{LF} and ξ_{LF}, respectively. When the pressure increases above 160 MPa (i.e., EPW2), ξ_{LF} shows a rapid increase while l_{LF} decreases. At the pressure $P\sim165$ MPa, ξ_{LF}, and l_{LF} are estimated to be 40 nm and 2 nm, respectively. The coverage Γ, calculated from the parameters $d_l^{\mathrm{FL}}(0)$, l_{FL}, and ξ_{LF} [the open circles in the Fig. 16(c)] is larger than that calculated from the slab model, because the long-range tail of the density profile is included in the former calculation.

A possible explanation for the rapid increase of ξ_{LF} may be a crossover from the prewetting to the critical adsorption [5]. In the low-pressure region where the correlation length of the bulk fluid phase is much smaller than the thickness of the wetting film, the density profile of the wetting film is well represented by the slab model. However, when the pressure is increased above the line EPW2, and the bulk critical point is approached, the bulk correlation length becomes large, and the density profile is governed by the bulk correlation length. Then the character of the wetting film could be changed from two dimensional to three dimensional.

An alternative explanation for the anomaly at EPW2 may be that it is driven by the change in the long-range force between a mercury atom and the sapphire substrate. As stated in Sec. IV B, the van der Waals chemical potential is expressed by Eq. (4.4), which contains the adsorbate-substrate, the adsorbate-adsorbate, and the various many-body interactions [22]. For simplicity, we restrict ourselves to a discussion of only the adsorbate-substrate interaction, or, the direct interaction between the mercury atom and the sapphire substrate without the wetting film. When there is no wetting film on the substrate, the van der Waals energy of a mercury atom at a distance R from the substrate is expressed in terms of the electric polarizability α of the atom, the dielectric constant ϵ_{sub} of the substrate, and the dielectric constant ϵ_{gas} of the surrounding mercury vapor at imaginary frequencies $i\omega$ [23]:

$$W=-\frac{\hbar}{4\pi R^3}\int_0^{\infty} d\omega\,\alpha(i\omega)\frac{\epsilon_{\mathrm{sub}}(i\omega)-\epsilon_{\mathrm{gas}}(i\omega)}{\epsilon_{\mathrm{sub}}(i\omega)+\epsilon_{\mathrm{gas}}(i\omega)}. \tag{4.7}$$

When the density increases beyond the line EPW2, this energy is expected to change its sign from negative to positive, because this line nearly coincides with the isochore line of 4.0 g/cm^3 for the bulk fluid mercury, and $\epsilon_{\mathrm{gas}}-\epsilon_{\mathrm{sub}}$ changes its sign from negative to positive, as shown in the Fig. 9(c). Therefore, above the line EPW2, the mercury atoms feel repulsive force from the substrate, although the total force including the many-body interactions [Eq. (4.4)] remains attractive. This change in the adsorbate-substrate interaction may cause the expansion or swelling of the wetting film, which results in the decrease of the effective slab density d_{slab} and the increase of the effective slab thickness l_{slab}. The change in the interaction may possibly weaken the confinement of the wetting film in the vicinity of the substrate, and the character of the wetting film may be changed from two dimensional to three dimensional, as is expected when ξ_{LF} increases.

When the pressure is increased further, Γ shows a maximum at about 165 MPa, and then decreases, probably due to the increase of d_{gas} [i.e., the second term of the Eq. (4.3)].

V. SUMMARY

We have developed a new technique for optical reflectance measurements in the 45° reflection geometry, which can be applied under high temperature and pressure near the critical point of mercury. By using this technique, we have performed optical reflectance measurements on a sapphire-

mercury interface, and confirmed the wetting transition of mercury on a sapphire substrate unambiguously. We have studied quantitatively the physical properties of the wetting film, such as the density profile, the thickness, and the coverage. As a first approximation, we used the slab model for the density profile of the wetting film. It was found that the density of the wetting film $d_{\rm slab}$ is much smaller than that of bulk liquid at the liquid-vapor coexistence curve. This result is consistent with the Lifshitz theory [16], from which we may predict that the sapphire substrate prefers wetting film with density lower than the metal-nonmetal transition.

When the temperature is close enough to T_{pw}^{c}, it was found that the effective slab density $d_{\rm slab}$ shows a sharp decrease as the pressure approaches the liquid-gas coexistence. As an alternative to the slab model, the reflectance data were analyzed by using the tanh-type model profile [Eq. (4.5)], and it is suggested that the anomalous behavior in $d_{\rm slab}$ is explained by the increase in $w_{\tanh}$, or the broadening of the density profile. It is found that the coverage Γ does not depend strongly on the model density profile, and is more reliable as an order parameter than the model-dependent individual parameters.

In the prewetting supercritical region, two types of anomalies EPW1 and EPW2 are observed in the reflectances, and they define the extension of the prewetting line. EPW1 is identified as an increase of the interfacial fluctuation in the wetting film from the strong anomaly in the optical emissivity. EPW2 is characterized by the sharp decrease of the effective slab density $d_{\rm slab}$ or the sharp increase of the correlation length $\xi_{\rm LF}$. Two possible mechanisms of the anomaly EPW2 are suggested. One is a crossover between the prewetting and the critical adsorption. The other possibility is that the anomaly is driven by the change in the long-range force between a mercury atom and the sapphire substrate.

ACKNOWLEDGMENTS

We would like to thank Professor F. Hensel, who has led the authors to the field of wetting phenomena. We also thank Professor S. Dietrich, Professor W. Freyland, and Dr. D. Nattland for helpful discussions. This work is partially supported by a grant-in-aid for Scientific Research (07236103, 09440135) from the Ministry of Education, Science, Sports, and Culture, Japan.

APPENDIX

In this appendix, we explain how we have calculated the optical reflectivity coefficients r_i $(i=s,p)$ for the wetting film with smoothly varying density profile $d_l(z)$, such as in Figs. 10(b) or 10(c). Here z is the coordinate normal to the sapphire-mercury interface, which is located at $z=0$. Such a continuously varying dielectric media is often treated as a multilayer system, replacing the continuous profile by a steplike profile of N isotropic layers, and the reflectivity coefficients are calculated from the interference of the waves reflected from successive interfaces of the layers [24,25]. In the present paper, instead, we solved ordinary differential equations, which are derived from the Maxwell's equations for the continuously varying dielectric media, and this formulation is more suitable to the well-established numerical methods than the multilayer formulation.

We consider that fluid mercury with z-dependent complex refractive index $\tilde{n}(z)$ occupies the half-space $z>0$, and that sapphire with constant refractive index n_0 occupies the region $z\leqslant 0$. It should be noted that $\tilde{n}(z)-1$ is not proportional to the density $d_l(z)$ in the case of fluid mercury, unlike ordinary insulating substances. In this calculation, we assumed that the $\tilde{n}(z)$ at each z is determined from $d_l(z)$ by using the function shown in the Fig. 9(b).

Let us consider that the plane of incidence is the xz plane, and the incident light comes from the $z<0$ (sapphire) side at an angle θ to the z axis (in our case $\theta=45°$). The x component of the wave vector is $k_x=(2\pi/\lambda)n_0\sin\theta$, where λ is the wavelength of the light in the vacuum.

In general, the propagation of an electric field $\mathbf{E}(\mathbf{r})$ in a dielectric medium described by $\tilde{\epsilon}(z)=\tilde{n}(z)^2$, is determined by Maxwell's equations

$$\nabla\times\nabla\times\mathbf{E}(\mathbf{r})-(2\pi/\lambda)^2\tilde{\epsilon}(z)\mathbf{E}(\mathbf{r})=\mathbf{0}.$$

In the case of the s wave, the polarization vector is perpendicular to the plane of incidence, or, along the y axis $\mathbf{e}_y$ and $\mathbf{E}(\mathbf{r})$ has the form $\mathbf{E}(\mathbf{r})=E(z)e^{ik_x x}\mathbf{e}_y$. Then, $E(z)$ is calculated from the differential equation

$$d^2E(z)/dz^2+q(z)^2E(z)=0,$$

with

$$q(z)^2=(2\pi/\lambda)^2[\tilde{\epsilon}(z)-n_0^2\sin^2\theta].$$

In the case of the p wave, on the other hand, the electric field satisfies more complicated coupled partial differential equations for its x and z components. Instead, we used the corresponding magnetic field $\mathbf{B}(\mathbf{r})$, which satisfies Maxwell's equations

$$\nabla\times\left(\frac{1}{\tilde{\epsilon}(z)}\nabla\times\mathbf{B}(\mathbf{r})\right)-(2\pi/\lambda)^2\mathbf{B}(\mathbf{r})=\mathbf{0}.$$

For the p wave, $\mathbf{B}(\mathbf{r})$ is along $\mathbf{e}_y$, and $\mathbf{B}(\mathbf{r})=B(z)e^{ik_x x}\mathbf{e}_y$ is calculated from

$$\frac{d}{dz}\left(\frac{1}{\tilde{\epsilon}(z)}\frac{dB(z)}{dz}\right)+\frac{q(z)^2}{\tilde{\epsilon}(z)}B(z)=0.$$

These second-order differential equations can be rewritten as first-order differential equations by using the following matrix representations:

$$\frac{dG(z)}{dz}+A(z)G(z)=0.$$

In the case of the s wave, $G(z)$ and $A(z)$ are defined as

$$G(z)=\begin{pmatrix} E(z) \\ dE(z)/dz \end{pmatrix} \quad \text{and} \quad A(z)=\begin{pmatrix} 0 & -1 \\ q(z)^2 & 0 \end{pmatrix},$$

and for the *p*-wave,

$$G(z)=\begin{pmatrix} B(z) \\ [1/\tilde{\epsilon}(z)][dB(z)/dz] \end{pmatrix} \quad \text{and}$$

$$A(z)=\begin{pmatrix} 0 & -\tilde{\epsilon}(z) \\ q(z)^2/\tilde{\epsilon}(z) & 0 \end{pmatrix}.$$

When a boundary condition $G(z=0)$ is given, $G(z)$ for any z is calculated by integrating the above equations numerically. We used the fourth-order Runge-Kutta method for these calculations [26]. The solution $G(z)$ is related to the boundary condition $G(0)$ by using a transfer matrix $M(z)$, which is defined as $G(z)=M(z)G(0)$.

The boundary conditions for the reflectivity calculations are

$$E(z) \ [\text{or} \quad B(z)] = \begin{cases} P(e^{iq_< z}+r_i e^{-iq_< z}) & \text{for } z\leqslant 0 \ \ (i=s,p) \\ Qe^{iq(z_c)z} & \text{for } z\geqslant z_c, \end{cases}$$

where $q_<=(2\pi/\lambda)n_0\cos\theta$ is the z component of the wave vector in the region $z\leqslant 0$ (sapphire), and P, Pr_i, and Q are amplitudes of the incident, reflected, and transmitted lights, respectively. z_c is the cutoff, where the dielectric constant $\tilde{\epsilon}(z_c)$ becomes nearly equal to that of the bulk-gas phase. In the case of the tanh-type density profile [Eq. (4.5)], for example, we put $z_c=l_{\tanh}+3w_{\tanh}$, where $[d_l(z_c)-d_{\text{gas}}]/[d_l(0)-d_{\text{gas}}]$ is smaller than 0.005.

These boundary conditions are rewritten in the matrix representation as

$$G(0)=PL_i\begin{pmatrix} 1 \\ r_i \end{pmatrix},$$

$$G(z_c)=Q\begin{pmatrix} 1 \\ ig_i \end{pmatrix} \quad (i=s,p),$$

where

$$L_s=\begin{pmatrix} 1 & 1 \\ iq_< & -iq_< \end{pmatrix}, \quad L_p=\begin{pmatrix} 1 & 1 \\ iq_</n_0^2 & -iq_</n_0^2 \end{pmatrix}$$

and

$$g_s=q(z_c), \quad g_p=q(z_c)/\tilde{\epsilon}(z_c).$$

Note that $G(z)$ is continuous at $z=0$, thus the above boundary condition for $G(0)$ is valid on the both sides of the sapphire-mercury interface.

By using the boundary condition at $z=0$, one can obtain

$$G(z_c)=M(z_c)G(0)=PM(z_c)L_i\begin{pmatrix} 1 \\ r_i \end{pmatrix}=PN(z_c)\begin{pmatrix} 1 \\ r_i \end{pmatrix}.$$

Here, we put

$$M(z_c)L_i\equiv N(z_c)=\begin{pmatrix} n_{11} & n_{12} \\ n_{21} & n_{22} \end{pmatrix}.$$

Then, by comparing this solution with the boundary condition at $z=z_c$,

$$Q=P(n_{11}+r_i n_{12}),$$

$$Qig_i=P(n_{21}+r_i n_{22}).$$

The condition that P and Q have a nontrivial solution is

$$\begin{vmatrix} n_{11}+r_i n_{12} & -1 \\ n_{21}+r_i n_{22} & -ig_i \end{vmatrix}=0.$$

Thus, the reflectivity coefficients r_i $(i=s,p)$ are obtained as

$$r_i=-\frac{n_{21}-in_{11}g_i}{n_{22}-in_{12}g_i}.$$

[1] J. W. Cahn, J. Chem. Phys. **66**, 3667 (1977).

[2] M. Yao and F. Hensel, J. Phys.: Condens. Matter **8**, 9547 (1996).

[3] F. Hensel and M. Yao, Eur. J. Solid State Inorg. Chem. **34**, 861 (1997); F. Hensel and M. Yao, Ber. Bunsenges. Phys. Chem. **102**, 1798 (1998).

[4] Y. Ohmasa, Y. Kajihara, H. Kohno, Y. Hiejima, and M. Yao, J. Phys.: Condens. Matter **12**, A375 (2000).

[5] S. Dietrich, in *Phase Transitions in Surface Films 2*, edited by H. Taub, G. Torzo, H. J. Lauter, and S. C. Fain, Jr. (Plenum, New York, 1991), p. 391.

[6] F. Hensel and W. W. Warren Jr., *Fluid Metals* (Princeton University, New York, 1999), Chap. 4.

[7] Y. Ohmasa, Y. Kajihara, and M. Yao, J. Phys.: Condens. Matter **10**, 11 589 (1998).

[8] Y. Ohmasa, Y. Kajihara, H. Kohno, Y. Hiejima, and M. Yao, J. Non-Cryst. Solids **250-252**, 209 (1999).

[9] W. Götzlaff, Doctoral thesis, University of Marburg, 1988.

[10] T. Inagaki, E. T. Arakawa, and M. W. Williams, Phys. Rev. B **23**, 5246 (1981).

[11] R. M. A. Azzam and N. M. Bashara, *Ellipsometry and Polarized Light*, paperback edition (North-Holland, New York, 1987), Chap. 4.

[12] E. H. Hauge and M. Schick, Phys. Rev. B **27**, 4288 (1983).

[13] M. Yao, K. Takehana, and H. Endo, J. Non-Cryst. Solids **156-158**, 807 (1993).

[14] F. Hensel, J. Non-Cryst. Solids **117-118**, 441 (1990).

[15] D. E. Logan and P. P. Edwards, Philos. Mag. B **53**, L23 (1986).

[16] F. Hensel and W. W. Warren Jr., *Fluid Metals* (Princeton University, New York, 1999), Chap. 6.4.

[17] I. E. Dzyaloshinsky, E. M. Lifshitz, and I. P. Pitaevskii, Adv. Phys. **10**, 165 (1961).

[18] W. Hefner, Doctoral thesis, University of Marburg, 1980; W. Hefner, R. W. Schmutzler, and F. Hensel, J. Phys. (Paris), Colloq. **41**, C8-62 (1980).
[19] A. J. Liu and M. E. Fisher, Phys. Rev. A **40**, 7202 (1989).
[20] M. E. Fisher and P.-G. de Gennes, C. R. Seances Acad. Sci., Ser. B **287**, 207 (1978).
[21] M. E. Fisher and J.-H. Chen, J. Phys. (France) **46**, 1645 (1985).
[22] E. Cheng and M. W. Cole, Phys. Rev. B **38**, 987 (1988).
[23] A. D. McLachlan, Mol. Phys. **7**, 381 (1964).
[24] M. Born and E. Wolf, *Principles of Optics*, 6th ed. (Pergamon, New York, 1980), Chap. I.
[25] B. Heidel and G. H. Findenegg, J. Chem. Phys. **87**, 706 (1987).
[26] W. H. Press, S. A. Teukolsky, W. T. Vetterling, and B. P. Flannery, *Numerical Recipes in Fortran 77*, 2nd ed. (Cambridge University, New York, 1992), Chap. 16.